

# FLARE EXPANSION TO A MAGNETIC ROPE ACCOMPANIED BY RARE RADIO BURSTS

ALENA ZEMANOVÁ,<sup>1</sup> MARIAN KARLICKÝ,<sup>1</sup> JANA KAŠPAROVÁ,<sup>1</sup> AND JAROSLAV DUDÍK<sup>1</sup>

<sup>1</sup>*Astronomical Institute of the Academy of Sciences of the Czech Republic  
Fričova 298, CZ-25165 Ondřejov, Czech Republic*

## ABSTRACT

We present multispectral analysis (radio, H $\alpha$ , UV/EUV, and hard X-ray) of a confined flare from 2015 March 12. This flare started within the active region NOAA 12 297 and then it expanded into a large preexisting magnetic rope embedded with a cold filament. The expansion started with several brightenings located along the rope. This process was accompanied by a group of slowly positively drifting bursts in the 0.8–2 GHz range. The frequency drift of these bursts was 45 – 100 MHz s<sup>-1</sup>. One of the bursts had an S-like form. During the brightening of the rope we observed an unique bright EUV structure transverse to the rope axis. The structure was observed in a broad range of temperatures and it moved along the rope with the velocity of about 240 km s<sup>-1</sup>. When the structure dissipated, we saw a plasma further following twisted threads in the rope. The observed slowly positively drifting bursts were interpreted considering particle beams and we show that one with the S-like form could be explained by the beam propagating through the helical structure of the magnetic rope. The bright structure transverse to the rope axis was interpreted considering line-of-sight effects and the dissipation-spreading process, which we found to be more likely.

*Keywords:* plasmas – Sun: flares – Sun: radio radiation

## 1. INTRODUCTION

Solar flares are generally classified as either eruptive or confined (Fletcher et al. 2011). In X-ray or EUV observations the eruptive flares are characterized by a cusp-shaped magnetic structure above the flare arcade, while the confined flares have only a simple loop structure. The eruptive flares are usually related to an unstable and rising magnetic flux rope below which the current sheet is formed, where the magnetic reconnection takes place. The eruptive flares are connected with coronal mass ejections while confined flares are not. The eruptive flares were often described by the "standard" CSHKP flare model (Carmichael 1964; Sturrock 1966; Hirayama 1974; Kopp & Pneuman 1976), while recently a more general 3-dimensional model involving slipping magnetic reconnection was introduced (Aulanier et al. 2012, 2013; Janvier et al. 2013). Contrary to that, the confined flares are explained by the loop flare model, in which the energy release occurs inside the loop (Spicer

1977) or by the model describing interaction of current-carrying loops (Melrose 1997). Recently, two types of confined flares were introduced by Li et al. (2019). The confined flares of the first type are characterized by more complex magnetic configuration with strong shears, they involve a stable filament and slipping magnetic reconnection. The second type of confined flares has an unstable filament that erupts but is still confined by a strong strapping field and the reconnection occurs in an antiparallel magnetic field below the filament. Thus, the confined flares could be associated with appearance of a cusp structure as the eruptive ones; however, such observations are still rare in the literature (Liu et al. 2014; Gou et al. 2015; Hernandez-Perez et al. 2019).

The flaring process is not stationary but involves expansion of the flaring structure into the neighboring regions. For example, the well-known flare-ribbon motions in the perpendicular and/or parallel direction to flare ribbons are the most common types of expansions (e.g., Fletcher et al. 2011; Qiu et al. 2017), when surrounding coronal structures undergo magnetic reconnection progressively. Sometimes, the flaring activity can lead to the so-called domino effect, when after a flare at one location, other flares in the close locations appear (Zuccarello et al. 2009). Flare ribbons observed at a remote site from the main flaring loops are also observed in the connection with circular ribbon flares (e.g. Masson et al. (2009); Wang & Liu (2012); Liu et al. (2019, 2020); Devi et al. (2020)). Such flares are connected to the fan-spine magnetic topology, which is also intrinsic to coronal jets (Pariat et al. 2015; Wyper & DeVore 2016; Wyper et al. 2016). But an expansion of a flare into the preexisting magnetic rope as in the present case is a rare phenomenon according to our knowledge.

Radio emission is an integral part of solar flares and observed in various frequency ranges and on time scales from fractions of seconds up to hours. During flares different types of radio bursts (II, III and IV) and their fine structures can be observed (Krueger 1979; McLean & Labrum 1985). Among them the most common are type III bursts that are observed at frequencies from about 100 kHz to 1 GHz and drift to lower frequencies. They are considered to be a signature of the electron beams propagating through the solar atmosphere to the interplanetary space. A review of type III bursts is provided by Reid & Ratcliffe (2014).

Surveys of radio bursts in decimetric wavelengths is presented in papers by Isliker & Benz (1994) and Jiříčka et al. (2001), within 1–3 GHz and 0.8–2.0 GHz frequency ranges, respectively. Some of these bursts are still not well understood. This is a case of the slowly positively drifting bursts (SPDBs). They appear in groups or as single bursts, with a duration of an individual burst from 1 to several seconds and their frequency drift is lower than about  $100 \text{ MHz s}^{-1}$  (Jiříčka et al. 2001). The SPDBs seem to be similar to the reverse type III bursts (Aschwanden 2002) but their frequency drift is much smaller. The majority of observed SPDBs are connected to solar flares (Jiříčka et al. 2001), and they appear many times at the very beginning of the flares (Benz & Simnett 1986; Kotrč et al. 1999; Kaltman et al. 2000; Karlický et al. 2018). Kaltman et al. (2000) reported on several SPDBs observed during 3 solar flares in the 0.8–2 GHz frequency range. They found frequency drifts of the observed SPDBs to be within the  $20\text{--}180 \text{ MHz s}^{-1}$  range. Kotrč et al. (1999) studied one of those flares. By combining the radio and spectral plus imaging  $\text{H}\alpha$  observations, they explained the observed SPDBs as radio emission generated by downwards propagating shock waves. Based on numerical simulations of the formation of thermal fronts in solar flares, Karlický (2015) proposed that SPDBs observed in the 1–2 GHz range could be a signature of a thermal front. Furthermore, Karlický et al. (2018) reported about the observation of an SPDB (1.3–2.0 GHz) observed during the impulsive phase of an eruptive flare. They found time coincidence between the SPDB occurrence,

an appearance of an UV/EUV multi-thermal plasma blob moving down along the dark  $H\alpha$  loop at approximately  $280 \text{ km s}^{-1}$ , and the observed change of  $H\alpha$  profile at the footpoint of that dark loop. Combining these observations they concluded that observed SPDB was likely generated by the thermal front formed in front of the falling EUV blob.

Moreover, in the 230–350 MHz range Benz & Simnett (1986) showed five slowly drifting type III bursts with very low frequency drifts ( $-16$  to  $-41 \text{ MHz s}^{-1}$ ), connected to hard X-ray flare emissions. They argued that these bursts cannot be explained by the electron beams considered for typical type III bursts. They proposed that possible exciters could be proton beams. Simnett (1995) studied the role of protons during the flares and he argued that the bursts with slow drift rates and duration of seconds can be manifestations of the proton beams with energies well below the  $\gamma$ -ray production threshold.

In the present paper we analyze an M1.4 class flare of 2015 March 12, which started in the active region (AR) NOAA 12 297 and then it expanded into a large preexisting neighboring magnetic rope embedded with a cold filament. This expansion was connected with a formation of the cusp structure and an unusual EUV bright structure transverse to the rope axis. During this process rare SPDBs, including a unique one with an S-like form, were observed. Therefore, we analyze this flare in detail, especially the rare process of plasma expansion into the preexisting magnetic rope, and investigate the circumstances under which SPDBs occur and what agent can be responsible for their origin.

The paper is structured as follows. In Section 2, we present the data used in this study, Section 3 describes the evolution of the flare in radio,  $H\alpha$ , UV/EUV, and hard X-rays. In Section 4 we provide interpretation and discussion and finally in Section 5 we present our conclusions.

## 2. DATA

In this study we used full disk Sun images provided by the Atmospheric Imaging Assembly (AIA) (Lemen et al. 2012) on a board the *Solar Dynamic Observatory* (SDO) (Pesnell et al. 2012) acquired during the 11:30–13:00 UT time interval. AIA provides images of the Sun in 7 EUV filters (94, 131, 171, 193, 211, 304, and  $335 \text{ \AA}$ ), plus two UV filters (1600 and  $1700 \text{ \AA}$ ), and WL continuum. The cadence of the data was 12s and spatial resolution of  $1.5''$ . The AIA data were processed using the standard Solar Software (SSW) routine *aia\_prep.pro* and the stray-light has been removed by the method of Poduval et al. (2013).

*Reuven Ramaty High Energy Solar Spectroscopic Imager* (RHESSI) observed the impulsive phase of the M1.4 class flare during the time interval 12:08–12:14 UT and part of its late gradual phase at 12:34–13:10 UT. RHESSI data were used to synthesize hard X-ray images by VIS\_CS algorithm (Felix et al. 2017) in standard energy channels: 6–12, 12–25, 25–50 keV with temporal cadence of 20s. We also used the soft X-ray observations made by *Geostationary Operational Environmental Satellite 15* (GOES 15)<sup>1</sup>.

In radio band we analyzed observations from the 800–2000 MHz Ondřejov radiospectrograph with the time resolution 0.01 s (Jiříčka et al. 1993; Jiříčka & Karlický 2008).

To show the line-of-sight magnetic field of the AR NOAA 12 297, we used the full disk magnetograms acquired by the Helioseismic and Magnetic Imager (HMI) on *SDO* during 11:30–13:00 UT time interval. We used full disk magnetograms with cadence of 45s and spatial resolution of  $1''$ .

<sup>1</sup> [www.nasa.gov/content/goes-overview/index.html](http://www.nasa.gov/content/goes-overview/index.html)

For complementary imaging observations we used data produced by an X-ray Telescope (XRT) on board the *Hinode* mission and groundbased synoptic H $\alpha$  images provided by Global Oscillation Network Group<sup>2</sup> (GONG) Program. The XRT observed flaring activity within 11:39–12:28 UT time interval, with spatial resolution of about 2". The XRT data were processed by standard SSW routine *xrt\_prep.pro* but their coalignment was manually corrected to match AIA 131 Å images. The GONG H $\alpha$  network obtains the synoptic images using H $\alpha$  filters with bandpass of 0.5–0.6 Å and the nominal resolution of 2". It provides H $\alpha$  data covering the whole AIA time interval from several stations but not always with a good seeing conditions. In this study we used H $\alpha$  data observed at Cerro Tololo station which were already preprocessed by the provider<sup>3</sup> but lack the images during 12:19:34–12:25:34 UT time interval. Further, the H $\alpha$  images were manually coaligned with *SDO*/AIA 304 Å filter images.

### 3. THE EVOLUTION OF M1.4 FLARE

In the AR NOAA 12 297 on 2015 March 12 two subsequent flares were observed: M1.6 SOL20150312T11:50:00 and M1.4 SOL20150312T12:14:00. The M1.4 flare, appeared during a gradual phase of the previous M1.6 class flare, see Figure 1, where the GOES 15 X-ray fluxes and their time derivatives are plotted. While the first flare was spectroscopically analyzed in several papers using the Interface Region Imaging Spectrograph (IRIS) (Brannon 2016; Tian et al. 2016; Tian & Chen 2018), the second flare, according to our knowledge, has not been studied yet. This flare started within the same AR but later it expanded into a large preexisting magnetic rope outside the AR. This expansion was associated with rarely observed slowly positively drifting bursts in the 0.8–2.0 GHz range with one having an S-like form and an unusual EUV structure transverse to the rope axis. In the following, the evolution of the M1.4 flare in radio, H $\alpha$ , EUV, and X-rays is described.

#### 3.1. Radio observations

Figure 2(a) shows the 800–2000 MHz radio spectrum observed during the 12:09–12:13 UT time interval. The first weak bursts appeared in the 0.95–1.1 GHz range at about 12:09:16 UT, i.e. at the beginning of the flare impulsive phase. Then, a group of the slowly positively drifting bursts (SPDBs) was observed at about 12:10:20 – 12:12:30 UT in the whole 0.8–2 GHz range. These bursts are rare as shown in the statistics of radio bursts and their fine structures (Jiříčka et al. 2001) and their origin is unknown so far. They remind the reverse (RS) type III bursts but their frequency drift is much smaller. While the typical frequency drift of the RS type III bursts in the present frequency range is about  $\pm 1 \text{ GHz s}^{-1}$  (Aschwanden 2002), the frequency drift of those SPDBs is in the 45–100 MHz s<sup>-1</sup> interval. Moreover, in comparison to the RS type III bursts which appear on the spectrum more or less as a straight line, some of the SPDBs observed here are curved. For example, see the burst marked by S in Figure 2(b) at 12:10:34 – 12:10:41 UT in the 1000–1700 MHz range, which has an unusual S-like form. Such a shape of SPDB was observed for the first time. Further in the text we will refer to this burst as to the Burst S. Note, that these are not S-bursts (Solar Storm burst) observed in metric frequency range (McConnell 1980, 1982).

<sup>2</sup> <https://gong.nso.edu/>

<sup>3</sup> <https://www.nso.edu/data/nisp-data/h-alpha/>

### 3.2. Flare evolution in EUV, X-rays, and $H\alpha$

As our radio spectrum does not provide us with spatial information about radio source locations, we turn to investigate the origin of these specific SPDBs by following the evolution of the M1.4 flare in EUV, X-rays, and  $H\alpha$  images to search for any exceptional phenomena that could be connected to the observed bursts.

The M1.4 flare occurred during the gradual phase of the M1.6 flare. The M1.6 flare occurred at the northern part of AR NOAA 12 297 (Figure 3). During its peak phase an arcade (A) of bright flare loops appeared in EUV (Figure 4(a)). In  $H\alpha$  (Figure 4(b)) we observed two bright ribbons belonging to the arcade A: RN located in negative polarity N and RP in positive polarity spot P (see Figure 3(a)). We observed also two large systems of flare loops LS1 and LS2 associated with this flare. They were rooted at the east side of A, having their conjugate footpoints connected to two distinct locations within the AR (Figure 4(a)). These fading loops and A of M1.6 flare were present during the whole M1.4 flare.

The M1.4 flare occurred at the southern part of the AR (Figure 4(a) and (b)). Its impulsive phase was accompanied by SPDBs (Figure 1(b)). It involved a magnetic rope of the huge EUV filament (F) (Figure 3(b)) lying westward of AR NOAA 12 297. The F is observed in *SDO/AIA* 304 Å filter (Figure 3(b)) as well as in  $H\alpha$  (Figure 4) but in 304 Å it was much more extended.

At the beginning of M1.4 flare a new pair of J-shaped ribbons, R1 and R2, appeared to the southwest of A. They were connected by an EUV loop that started to rise (see the the animation accompanying Figure 4). The R1 was located in positive polarity of sunspot P, starting very close to RP of A, and the negative polarity ribbon R2 was located about 100" west from it (Figure 4(b)). At about 12:09 UT we observed a brightening at the elbow of the hook of R2 (Figure 4(a), accompanied by a *RHESSI* X-ray source (Figure 4(b)). The X-ray source continually moved along the hook of R2 toward its tip (Figures 4(b)–(d)–(f)). Simultaneously, a brightening at the conjugate hook of R1 appeared and was also accompanied by moving X-ray source (Figure 4(b)–(d)–(f)). For clarity, the observed X-ray sources located within the hooks of J-shaped ribbons R1 and R2 are pointed by black arrows in Figure 4(d). The X-ray source observed in the hook of R1 (Figure 4(b)–(d)–(f), orange contour) did not move as much as the one in R2. An additional soft X-ray source located over the ribbon RN (Figure 4(b) and (d), green contour) did not belong to the M1.4 flare. It represents emission from hot flare loops belonging to A.

Slightly earlier, from about 12:08 UT, several regions bright in EUV started to appear along F, lying westward of AR NOAA 12 297 (Figures 4(a) and (b) and see the animation accompanying Figure 4).

After 12:10 UT, the loops connecting R1 and R2 became brighter in EUV and we observed a thin stripe of plasma coming out of the tip of the hook of R2, see the smaller rectangle in Figure 4(c). Later, a small cusp appeared at the tip of R2 (Figure 4(e)). Its position is marked by a red square in Figures 4(e) and (f). The large rectangle in Figure 4(c) indicates the position of a bulk of heated plasma which brightened over the F (Figure 4(d)). Figure 4(e) shows that heated plasma, located over F, formed a bright emission structure seen in the 131 Å filter (circle). The structure was narrow and oriented transverse to the axis of F. We will refer to this structure as to the bright transverse structure (BTS). Figure 4(f) shows that part of the BTS cloud be seen in emission also in  $H\alpha$  (circle). At about 12:12:30 UT, a new hard X-ray source also appeared over R1 (red contour, Figure 4(f)).

The narrow BTS appeared to move along the filament axis. Simultaneously, a new ribbon appeared at the end of EUV filament (red square of Region 6, Figure 4(e)). Following 12:12:30 UT the narrow BTS started to dissipate and increased its width. In the gradual phase of the flare we already observed a bulk of heated plasma following the twisted filament threads (Figure 4(g)) and several new flare loops were created: within the AR (black arrow), below the cusp and also longer ones at other places (yellow arrows). In  $H\alpha$  we observed changes in appearance of dark filament threads compared to the situation at the beginning of the flare (see Figure 4(h) and (b) and see the animation accompanying Figure 4).

As has been described in subsection 3.1, the main part of SPDBs was observed during the 12:10:20–12:12:30 UT time interval (Figure 2(a)). This corresponds well to the appearance of the cusp and formation of BTS. Therefore, we focus on these phenomena in the following subsection.

### 3.2.1. *The cusp, BTS, and flare loops*

Formation of the cusp and ejection of plasma toward the F is documented in Figures 5 and 6. In particular, this part of the flare evolution was accompanied by the main part of SPDBs at 12:10:20 – 12:12:30 UT (Figure 2(a)). Among these bursts, the Burst S with S-like form was observed at 12:10:34 – 12:10:41 UT (Figure 2(b)).

Figure 5 shows the sequence of *SDO*/AIA base difference images during the time of the Burst S. Circles show the central part where we can follow the formation of new loops filled with plasma ejected toward F. On the left side of the circle in Figure 5(a), we observed hot loops reaching its central area, while on the upper right side we saw a new flare loop to form (upper arrows in Figure 5(b) and (f)). Formation of another flare loop can be followed in Figures 5(f)–(h), at the lower side of the circles (arrows). At 12:10:44 UT, just three seconds after the Burst S, we observed there two small brightenings there (Figure 5(f) and (g)). The left one (Figure 5(g), arrow) was located at the area where, in  $131 \text{ \AA}$ , we saw bright loops crossed by other tiny bright loop (Figure 5(c), arrow). Afterwards, both brightenings disappeared and we observed the second new loop with heated plasma ejected toward F (Figure 5(d) and (h), arrows). Thus, the Burst S occurred when we observed plasma ejection toward the F.

The flare evolution then continues in Figure 6. Panels (a) and (e) show the plasma coming out from the forming cusp after the Burst S (arrows). Figure 6(i) shows the F and  $H\alpha$  brightenings in Regions 1–3. The cusp itself was fully developed a couple of seconds later (Figure 6(b)–(f)–(j), red circles). The detailed view of the cusp can be seen in Figure 7. In the hot channels of *SDO*/AIA  $131 \text{ \AA}$  ( $\log T [K] = 7.05 - 7.15$ , O’Dwyer et al. (2010)) and *Hinode*/XRT Be\_thin filter ( $\log T [K] = 6.50 - 6.60$ , O’Dwyer et al. (2014)), a structure can be resolved within the cusp: a bright area at the top and bright kernels in its legs (Figure 7(a) and (b)). The X-ray source (Figure 7(a)) was not located right at the cusp leg but slightly northeast of it. Figure 7(c) shows the same area in coronal emission originating at temperatures  $\log T [K] = 5.85 - 6.35$  (O’Dwyer et al. 2010). No cusp can be seen there. We observed there short flare loops connecting the ribbons of opposite polarity, and the flare loop coming out of the cusp (Figure 7(c), arrow). This flare loop is almost invisible in the Be\_thin filter (Figure 7(b), arrow), which is probably a consequence of short exposure time as the XRT was still following the previous flare.

At 12:11:34 UT in  $131 \text{ \AA}$  (Figure 6(f)), approximately at coordinate Solar-X=50'', we saw bright emission of plasma located over the preexisting  $H\alpha$  filament F (Figure 6(j)). This bright emission

started to form narrow BTS, which was moving along the axis of F. About 12:12 UT the narrow BTS was already formed (Figure 6(c)–(g)–(k), yellow circles). Behind the moving and dissipating BTS we observed a faint tail of hot plasma visible in Al<sub>L</sub>poly and 131 Å (Figure 6(d) and (h), arrows). Note that the narrow BTS existed approximately during 12:11:30–12:12:30 UT but we observed a lot of intensive SPDBs even earlier, at 12:10:50–12:12:10 UT (Figure 2(a)).

We studied the evolution of BTS by the method of time-distance plots (Figure 8). The yellow line in Figure 8(a) shows a cut used to construct a time-distance plot in Figure 8(b). The BTS started to form at about 12:11:30 UT and then it became a bright and narrow structure moving along the F (see the animation accompanying Figure 4). After 12:12:30 UT it started to dissipate (Figure 8(b)). The projected velocity of narrow BTS was estimated using time-distance plots as that in Figure 8(b), but constructed also for other *SDO*/AIA EUV filters, plus 1600 Å (not shown here). At all time-distance plots we measured the slope of the bright ridge seen between the dashed lines at 12:11:30–12:12:30 UT as is shown in Figure 8(b). The estimated velocities covered the interval 190–292 km s<sup>-1</sup>, with an average velocity of 240 ± 50 km s<sup>-1</sup>.

The emission of BTS could be seen in all AIA filters as well as in the H $\alpha$  filtergram (Figure 9 and Figure 6(c)–(g)–(k)). This indicates a presence of multi-thermal plasma. Using the method of Cheung et al. (2015) we estimated the emission measure per temperature bin  $EM_j$  in two small squared areas: in BTS and in the cusp (Figure 10(a)). For this purpose we used images of EUV *SDO*/AIA filters taken about 12:12:36 UT, excluding 304 Å. The adopted temperature interval was  $\log T [K] = 5.70 - 7.70$ , with bin width of 0.1. Although the chosen method of DEM inversion does not explicitly provide an error of calculated  $EM_j$ , it can give us a qualitative result. The average  $EM_j$  curves calculated for the areas in the cusp and BTS are shown in Figure 10(b). The black curve represents  $EM_j$  distribution for BTS and has a cutoff at about  $\log T [K] = 6.90$ . The peak appears at  $\log T [K] \sim 6.40$  but it also shows the presence of plasma with  $\log T [K] \lesssim 6.00$ . This corresponds with our observations (Figures 6(c)–(g)–(k) and Figure 9). The red curve is  $EM_j$  for the cusp. It shows a small peak at  $\log T [K] \sim 6.40$  but an order of magnitude larger amount of plasma at  $\log T [K] \sim 7.10$ . This means that primary heating occurred at the cusp and hot plasma was ejected toward cold magnetic rope F, where cooler but still multi-thermal BTS appeared.

After 12:12:30 UT no SPDBs were observed (Figure 2(a)). When narrow BTS dissipated, a bulk of heated plasma was seen to move along the axis of F (Figure 6(h)) and after 12:14 UT the individual threads started to appear within that bulk (Figure 8(b)). Figure 4(g) shows that in later gradual phase we saw heated plasma following the twisted threads of the magnetic rope F.

Figure 11(a) shows the base difference image of Figure 4(g). We depicted there parts of the bright twisted threads of F by yellow and red dots. It seems that most likely they connect Region 0 as far as to Region 6 (Figure 11(b)). So, the observations suggest that after magnetic reconnection occurred above the cusp, the twisted threads of the magnetic rope F reached closer to the center of the AR (Region 0). We also noticed further systems of flare loops (Figure 11(a)): within the AR (black arrow), below the cusp and also in the vicinity of Region 1 (yellow horizontal arrows). We used the observed activity in the preexisting magnetic rope F to track the changes in connectivity. We do it by analysis of light curves (LCs) of Regions 1–6.

The UV/EUV LC for brightenings observed along the F are shown in Figures 12(a) and (b). We added there also an LC for Region 0 that was located approximately at the position of the hard X-ray source observed inside the hook of R1 (Figure 4(b)). We did not construct the UV/EUV LC for

the hard X-ray source observed in the hook of R2 because it moved a longer distance along the hook. Then in UV/EUV such LC would not present a signal from a structure in a compact area as the other curves do. Each of the UV/EUV light curves was constructed for the time interval 12:00–13:00 UT and was normalized to its maximum within this interval. Figure 12(c) shows LCs for solar radio flux registered in 3 GHz (gyrosynchrotron emission), in 1.2 GHz (plasma emission mechanism), and in hard X-rays at 25–50 keV. Figure 12(d) shows LCs for individual hard X-ray sources observed in the hooks of ribbon R1 (blue) and R2 (red). At the bottom of each panel in the Figure 12 we put labels to mark the times when SPDBs and narrow BTS were observed. It seems that footpoints of the first flare loops, produced by early magnetic reconnection above the cusp, could be located in Regions 1, 2, 4, and 5. Their UV (1600Å) LCs (Figures 12(a)) show maxima or local maxima about 12:10 UT, which is about the first peak of 3 GHz and 25–50 keV emission (Figure 12(c)). At this time also weak SPDBs appear (Figure 12(c), orange curve). This is valid also for EUV LCs (Figures 12(b)) but the aforementioned maxima or local maxima are slightly shifted in time due to heating of plasma. About 12:12 UT the UV/EUV LCs for Regions 1 and 2 (Figures 12(a) and (b)) reached their maxima. This is when the second peak in 3 GHz occurs and when BTS forms and exists, and when the intensive SPDBs (Figure 12(c)) are observed. We have to note that at this time the Regions 1–5 were already contaminated by emission of flare loops seen in EUV. Further, both hard X-ray sources located within the hooks of R1 and R2 show small peaks before 12:10 UT (Figure 12(d)), during the first peak of 3 GHz emission. We can deduce that at this time of early reconnection they were still magnetically connected. But the hard X-ray source located in the hook of R1 exhibits the maximum of the LC at 12:11:30 UT and thus dominantly contributes to the second peak of global hard X-ray emission in Figure 12(c), appearing at the time of the second 3 GHz maximum. In UV/EUV the LC for the Region 0 corresponds to this source (Figures 12(a) and (b)). Finally, the UV/EUV LCs for Region 3 (Figures 12(a) and (b)) have different character compared to the other regions. They were continually rising and reached their maximum after 12:16 UT when plasma bulk passed through this region. It seems that this region likely represented a part of a loop. Contrary to Region 3, both UV and EUV LCs for Region 6 show the local maximum about 12:13 UT. This corresponds to the appearance of the flare ribbon there (Figure 4(e) and Figure 11(b)).

Summarizing the analysis of LCs, it comes out that at the beginning of the flare the hooks of R1 and R2 were connected by activated EUV loops (Figure 4(a)). Then, due to magnetic reconnection within the region above the cusp new flare loops appeared in vicinity of Regions 1 and 2 (Figure 4(g)) and a new connectivity was also established between Regions 0 and 6 (Figure 4(g)). The latter two regions represent the hook of R1 and the far end of the magnetic rope F (Figure 11(b)).

#### 4. INTERPRETATIONS AND DISCUSSIONS

In the previous section we analyzed the flare evolution with its expansion to the preexisting magnetic rope (Figure 4) and phenomena accompanied by unusual SPDBs (Figure 2). This section is dedicated to interpretation of our results and to their discussion.

Considering the existence of the hot cusp (Figure 7), ejection of heated plasma and appearance of BTS (Figures 6), all accompanied by SPDBs (Figure 2), we argue that all those phenomena are related to the process of magnetic reconnection. If the reconnection was the case, then it had to occur in the vicinity of the cusp, most likely in the region above it (Figure 5). Then, accelerated particles were ejected from the reconnection region and they followed the newly created field lines. Hitting the



lower atmosphere they produced new ribbons (Figure 4(e) and (f)). In accordance with this proposed scenario, we observed arcades of hot flare loops below the cusp (Figure 4(g)) and brightenings that appeared along the preexisting magnetic rope with the embedded filament outside the AR (Figure 4). The bright twisted threads (Figure 11) document the involvement of the large filament F.

Now a question arises: what is the origin of SPDBs that appeared at the beginning of the plasma expansion? According to their appearance in the radio spectrum, they resembled the RS type III bursts. But their frequency drift is much smaller. To learn more about these bursts, we analyzed the Burst S, the one with the S-like form (Figure 2(b)) in detail. Using the Aschwanden's model of densities of the solar atmosphere (Aschwanden 2002) and the assumption of the plasma emission on the fundamental frequency or on the second harmonic, the velocity of the particle beam generating Burst S is about 2040 and 3650 km s<sup>-1</sup>, respectively. Note that this velocity means the velocity in the vertical direction in the gravitationally stratified solar atmosphere. The corresponding plasma densities are  $1.23 \times 10^{10} - 3.56 \times 10^{10}$  cm<sup>-3</sup> (for the emission on the fundamental frequency) or  $3.08 \times 10^9 - 8.92 \times 10^9$  cm<sup>-3</sup> (for the emission on the harmonic frequency). The estimated velocities are too small for the electron beam considered in the (RS) type III bursts. We note that in the present 800-2000 MHz frequency range there is no systematic study of beam velocities for reverse type III bursts due to their high frequency drift and limited time resolution of radiospectrographs. Nevertheless, these velocities need to be greater than 0.15 *c* (Aschwanden 2002) and their typical velocity should be the same as for type III bursts, i.e. 0.3 *c* (Krueger 1979), where *c* is the speed of light, due to an expected symmetry in acceleration of beams in upward and downward directions in the solar atmosphere.

However, based on the simultaneous start of SPDBs and first brightenings along the preexisting magnetic rope, we assume that the beam propagates from the cusp region through the rope that is nearly horizontally oriented. In such a case the frequency drift can correspond to much higher beam velocities depending on the angle between the rope axis and the horizontal plane. This interpretation is supported by an unusual S-like form of Burst S. Namely, if the particle beam propagates along the helical structure of the nearly horizontal magnetic rope then such an S-like form of the burst can be expected. It looks that the S-like burst form corresponds to the beam trajectory with the  $2\pi$  twist angle.

We simulated this S-like form of the Burst S. We assumed the cylindrical magnetic rope with the length 210000 km, which roughly corresponds to the distance between the cusp and the detection point 5 in Figure 4(b). The axis of the rope has some small angle  $\alpha$  to the photospheric plane. The rope is embedded in the gravitationally stratified solar atmosphere, the density of which changes with the height scale corresponding to the temperature *T*;  $H_s[m] = 50 T[K]$  (Priest 1982). We suppose that in this cylindrical rope a particle beam moves downwards along the magnetic field line having the helical form with the radius *R* around the rope axis. Along its trajectory the beam generates the local electrostatic (Langmuir) waves by the beam-plasma instability. These waves are then transformed by nonlinear processes to the electromagnetic (radio) waves observed as the Burst S. Here, for simplicity we calculated beam trajectories only for the emission on the fundamental frequency. Duration of Burst S is 7s which gives the beam velocity parallel to the rope axis as  $v_{\parallel} = 30000$  km s<sup>-1</sup>. The result of the beam induced emission is shown in Figure 2(c) by the dashed line. A qualitative agreement with observations was found for the parameters shown in Table 1. In all these cases (A, B, and C) the same result (Figure 2(c)) was obtained. This shows that increasing the temperature *T* in the

Case	T (K)	Height scale $H_s$ (km)	$v_{\perp}/v_{\parallel}$	R (km)	$\alpha$ (degree)
A	$1.5 \times 10^5$	7500	0.02	670	2.2
B	$3.9 \times 10^5$	19500	0.05	1660	5.7
C	$1 \times 10^6$	50000	0.1	3330	14.3

**Table 1.** Parameters of the magnetic rope corresponding to the S-like form of Burst S.  $T$  is the temperature in the solar atmosphere,  $v_{\parallel} = 30000 \text{ km s}^{-1}$  and  $v_{\perp}$  is the velocity parallel and perpendicular to the rope axis,  $R$  is the radius around which the agent rotates in the helical magnetic rope, and  $\alpha$  means the angle between the rope axis and horizontal plane. All these cases give the same result (Figure 2(c)).

solar atmosphere and thus the height scale requires an increase of the radius  $R$ , the beam velocity  $v_{\perp}$  perpendicular to the rope axis, and increase of the angle  $\alpha$  between the rope axis and horizontal plane. Due to no additional information we cannot decide which case of A, B, and C is the most appropriate to observations.

Now, we first consider an electron beam as the beam generating Burst S. The Burst S lasts 7 s and is produced in relatively high plasma densities, where collisions are not negligible. Therefore, let us estimate the stop time for electrons with the velocity  $30000 \text{ km s}^{-1}$  in the plasma with the density of  $2.4 \times 10^{10} \text{ cm}^{-3}$  (the mean density in the Burst S source for the emission on the fundamental plasma frequency). (We note that the total velocities in the cases A, B, and C (Table 1) are slightly higher than  $30000 \text{ km s}^{-1}$  due to the presence of the small component perpendicular to the rope axis.) Using the relations (Karlický et al. 1990)

$$z_{\text{stop}} = \frac{E_0^2}{3K\Lambda n_e}, \quad (1)$$

$$t_{\text{stop}} = \frac{2z_{\text{stop}}}{v_0}, \quad (2)$$

where  $z_{\text{stop}}$  and  $t_{\text{stop}}$  are the stop distance and stop time for electrons with the initial energy  $E_0 = 1/2m_e v_0^2$ ,  $m_e$  is the electron mass,  $v_0$  is the initial electron velocity,  $K = 2\pi e^4$ ,  $e$  is the electron charge,  $\Lambda$  is the Coulomb logarithm, and  $n_e$  is the plasma density, we found that the stop time is 0.023 s. In the case, when the emission of Burst S is on the harmonic frequency, i.e., the electrons propagate in the plasma with the mean density of  $6 \times 10^9 \text{ cm}^{-3}$ , the stop time is 0.093 s. In the both cases the duration of Burst S is much longer than the beam stop time, that is why the electron beam would be destroyed in a shorter time than the duration of the Burst S is, and thus the electron beam cannot generate Burst S. Therefore, let us consider the proton or neutral (current neutralized) beam. The neutral beam is the beam of protons and electrons having the same velocity. It is formed in the beam-plasma system owing to the inductive electromagnetic effects (Simnett & Haines 1990).

Because for the both proton and neutral beams the stop time is mainly given by protons, we calculate the stop time only for the protons. Modifying the relations (1) and (2) by the factor  $1.5 m_p/m_e$  (Emslie 1978), where  $m_p$  is the proton mass, the stop time for the protons with the velocity  $30000 \text{ km s}^{-1}$  in the plasma with the mean density  $2.4 \times 10^{10} \text{ cm}^{-3}$  (the emission on the fundamental frequency) is 64.1 s and in the plasma with the mean density  $6 \times 10^9 \text{ cm}^{-3}$  (the emission on the harmonic frequency) is 256.3 s. Both the times are much longer than the duration of Burst S (7s). This means that the proton or neutral beam keeps its form during the time of Burst S (beams are not scattered during this time). Thus, these beams can generate the Langmuir

waves along their trajectory downwards in the solar atmosphere in a similar way as the electron beam (Karlický et al. 1998). The Langmuir (electrostatic) waves are then transformed by nonlinear processes into electromagnetic (radio) waves (Burst S), similarly as in models of type III bursts. After the generation of Burst S, the proton or neutral beam continues in its propagation downwards. However, in lower atmospheric layers conditions for generation of the Langmuir waves and/or their transformation to the radio waves and/or radio wave absorption/propagation are changed and thus no further radio emission is observed. Finally, when the proton or neutral beam enters to even deeper and more dense atmospheric layers, these beams are collisionally stopped. In such a way, we think that the proton or neutral beam can generate the Burst S. The energy of the protons in this case is 4.69 MeV. This agrees with the results presented by Benz & Simnett (1986). For the generation of radio bursts, the beams with the densities, which are several orders of magnitude smaller than the density of the background plasma, are sufficient (Melrose 1980). Therefore, no additional observational effects of such weak beams can be expected.

Because we have no information about positions of the SPDB radio sources and as during SPDBs several systems of flare loops were formed, a question arises if SPDBs are not connected to any of them. We cannot rule out this possibility. However, it is known that during an evolution of a flare, both shear (Aulanier et al. 2012) and twist (Sych et al. 2015) in the flare loops decrease and the magnetic field becomes more or less potential. Thus, in the flare loops the helical structure of the magnetic field, which is needed for the explanation of the S-like form of one SPDB, is not very probable. Moreover, systems of flare loops are frequently observed phenomenon but the SPDBs are rarely observed. Furthermore, first SPDBs appeared simultaneously with the first brightenings in the magnetic rope. Therefore, we think that the probability of locations of the SPDB sources in the flare loops is low.

BTS (Figure 6(g), (h), and Figure 8) is another interesting aspect of this flare. It evolved while the plasma followed the twisted loops of the magnetic flux rope (Figure 4(g)) and it appeared during some SPDBs. When a hot plasma expands into the location of preexisting magnetic rope, its expansion can be in principle described (a) as a simple plasma expansion into the passive magnetic field structure of the magnetic rope or (b) as the dissipation-spreading process (Norman & Smith 1978). In case (a) BTS could originate due to a projection effect along the line of sight. For example, a narrow structure could appear when a bulk of heated plasma is ejected along the highly twisted magnetic field lines of a flux rope, the axis of which is oriented almost perpendicular to the line of sight. To verify this possibility we estimated the angle of twisted loop compared to the rope axis observed in Figure 11(a) (yellow dots). We found the angle to be about 40 degrees and such an angle is not sufficient to produce a narrow structure in projection. Moreover, a highly twisted magnetic flux rope would be unstable and the observed one is stable. In case of (b), when considering the dissipation-spreading process, physically it means that during the expansion of hot flare plasma new energy-release processes appear at new locations within the preexisting magnetic rope. The dissipation process can spread owing to particle beams and/or magnetosonic waves (Karlický & Jungwirth 1989; Odrščil & Karlický 1997). In this case BTS could be formed due to an additional magnetic reconnection (triggered by a plasma expansion) between long loops of the magnetic rope and shorter loops that are transverse to the rope axis and located below the rope in the region close to BTS (Figure 6(b)–(c) and (f)–(g)). The magnetic reconnection heats the shorter loops and forms BTS. The kinetic pressure inside the loops of BTS increases and due to the ballooning instability (Shibasaki 2001) BTS expands and disrupts.

Then we see a motion of BTS and plasma motion after BTS disruption. This interpretation can be supported by the second 3 GHz maximum observed about 12:11:40 UT, i.e., at the time of BTS, which indicates some additional energy release as expected in the dissipation-spreading process.

In Karlický (2015) an example of one SPDB was presented in association with the falling bright EUV blob and  $H\alpha$  chromospheric response. That SPDB was interpreted as a radio signature of a thermal front. In the present case we find some similarities with those observations. During the occurrence of several strong SPDBs about 12:11–12:12 UT we observed bright and multi-thermal BTS (Figure 9) moving along a cold filament. The BTS had a rather broad EM(T) curve (Figure 10(b)) that peaked at  $\log T [K] = 6.4$ , i.e. at  $T \sim 2.5 \times 10^6$  K. Furthermore, the average value of estimated projected velocity of BTS,  $240 \pm 50 \text{ km s}^{-1}$ , corresponded to the sound speed in plasma with  $T \sim 2.5 \times 10^6$  K. However, in the present case, we did not observe any particular cold preexisting loops into which a hot plasma was injected, and few SPDBs, including Burst S, were registered before the BTS was formed (12:09:10–12:11:20 UT, Figure 2(a)). Moreover, it would be very difficult to explain the SPDB with the S-like form (Burst S) by the thermal front. We cannot exclude that the other SPDBs (except Burst S) were of different origin; however we suggest that all SPDBs are produced by proton beams.

## 5. CONCLUSIONS

We report on a rare observation of slowly positively drifting radio bursts (SPDBs) in the 0.8-1.2 GHz range. Since the radio spectrum does not provide any information about the location of radio source, we investigated the EUV and X-ray observations of the associated flare in order to search for their origin.

The flare started close to the sunspot within the active region and then it expanded into a huge preexisting magnetic rope with a cold filament. We found that this expansion was accompanied by SPDBs and the bright transverse structure to the rope axis (BTS).

We recognized the small cusp magnetic field structure during the impulsive phase of the flare that looks to be a source of the particle acceleration and plasma expansion into the rope. The unique SPDB with S-like form that occurred during this time was simulated by considering a propagation of the particle beam in the helical magnetic field structure of the rope, which is nearly horizontally oriented. This burst lasted 7 s in a relatively dense plasma, where the particle collisions are not negligible. Considering these collisions we interpret this burst as caused by the proton or neutral beam with energies about 4.7 MeV. Our interpretation is in a good agreement with the works by Benz & Simnett (1986) and Simnett (1995), who explain the slowly drifting type III bursts in a similar way.

Furthermore, during an expansion of the plasma into the preexisting magnetic rope we found an unusual narrow EUV bright structure located transverse to the rope axis BTS. This structure was observed in a broad range of temperatures and moved along the filament with the velocity of about  $240 \text{ km s}^{-1}$ . The formation and dissipation of this structure has been observed at times of some SPDBs, but their mutual relation remains unclear. The bright EUV structure was interpreted considering line-of-sight effects and the dissipation-spreading process, which we found more likely to occur.

## ACKNOWLEDGMENTS

We acknowledge support from the project RVO:67985815 and Grants: 18-09072S, 19-09489S, 20-09922J and 20-07908S of the Grant Agency of the Czech Republic. AIA and HMI data are provided courtesy of NASA/SDO and the AIA and HMI science teams. We thank the RHESSI team for providing the data and software support. Hinode is a Japanese mission developed and launched by ISAS/JAXA, with NAOJ as domestic partner and NASA and STFC (UK) as international partners. It is operated by these agencies in co-operation with ESA and NSC (Norway). This work utilizes GONG data from NSO, which is operated by AURA under a cooperative agreement with NSF and with additional financial support from NOAA, NASA, and USAF.

## REFERENCES

- Aschwanden, M. J. 2002, *SSRv*, 101, 1, doi: [10.1023/A:1019712124366](https://doi.org/10.1023/A:1019712124366)
- Aulanier, G., Démoulin, P., Schrijver, C. J., et al. 2013, *A&A*, 549, A66, doi: [10.1051/0004-6361/201220406](https://doi.org/10.1051/0004-6361/201220406)
- Aulanier, G., Janvier, M., & Schmieder, B. 2012, *A&A*, 543, A110, doi: [10.1051/0004-6361/201219311](https://doi.org/10.1051/0004-6361/201219311)
- Benz, A. O., & Simnett, G. M. 1986, *Nature*, 320, 508, doi: [10.1038/320508a0](https://doi.org/10.1038/320508a0)
- Brannon, S. R. 2016, *ApJ*, 833, 101, doi: [10.3847/1538-4357/833/1/101](https://doi.org/10.3847/1538-4357/833/1/101)
- Carmichael, H. 1964, *NASA Special Publication*, 50, 451
- Cheung, M. C. M., Boerner, P., Schrijver, C. J., et al. 2015, *ApJ*, 807, 143, doi: [10.1088/0004-637X/807/2/143](https://doi.org/10.1088/0004-637X/807/2/143)
- Devi, P., Joshi, B., Chandra, R., et al. 2020, *SoPh*, 295, 75, doi: [10.1007/s11207-020-01642-y](https://doi.org/10.1007/s11207-020-01642-y)
- Emslie, A. G. 1978, *ApJ*, 224, 241, doi: [10.1086/156371](https://doi.org/10.1086/156371)
- Felix, S., Bolzern, R., & Battaglia, M. 2017, *ApJ*, 849, 10, doi: [10.3847/1538-4357/aa8d1e](https://doi.org/10.3847/1538-4357/aa8d1e)
- Fletcher, L., Dennis, B. R., Hudson, H. S., et al. 2011, *SSRv*, 159, 19, doi: [10.1007/s11214-010-9701-8](https://doi.org/10.1007/s11214-010-9701-8)
- Gou, T., Liu, R., & Wang, Y. 2015, *SoPh*, 290, 2211, doi: [10.1007/s11207-015-0750-8](https://doi.org/10.1007/s11207-015-0750-8)
- Hernandez-Perez, A., Su, Y., Thalmann, J., et al. 2019, *ApJL*, 887, L28, doi: [10.3847/2041-8213/ab5ba1](https://doi.org/10.3847/2041-8213/ab5ba1)
- Hirayama, T. 1974, *SoPh*, 34, 323, doi: [10.1007/BF00153671](https://doi.org/10.1007/BF00153671)
- Islaker, H., & Benz, A. O. 1994, *A&AS*, 104, 145
- Janvier, M., Aulanier, G., Pariat, E., & Démoulin, P. 2013, *A&A*, 555, A77, doi: [10.1051/0004-6361/201321164](https://doi.org/10.1051/0004-6361/201321164)
- Jiříčka, K., & Karlický, M. 2008, *SoPh*, 253, 95, doi: [10.1007/s11207-008-9118-7](https://doi.org/10.1007/s11207-008-9118-7)
- Jiříčka, K., Karlický, M., Kepka, O., & Tlamicha, A. 1993, *SoPh*, 147, 203, doi: [10.1007/BF00675495](https://doi.org/10.1007/BF00675495)
- Jiříčka, K., Karlický, M., Mészárosová, H., & Snížek, V. 2001, *A&A*, 375, 243, doi: [10.1051/0004-6361:20010782](https://doi.org/10.1051/0004-6361:20010782)
- Kaltman, T., Karlický, M., & Jiříčka, K. 2000, *Hvar Observatory Bulletin*, 24, 35
- Karlický, M. 2015, *ApJ*, 814, 153, doi: [10.1088/0004-637X/814/2/153](https://doi.org/10.1088/0004-637X/814/2/153)
- Karlický, M., Alexander, D., Brown, J. C., & MacKinnon, A. L. 1990, *SoPh*, 129, 325, doi: [10.1007/BF00159044](https://doi.org/10.1007/BF00159044)
- Karlický, M., & Jungwirth, K. 1989, *SoPh*, 124, 319, doi: [10.1007/BF00156273](https://doi.org/10.1007/BF00156273)
- Karlický, M., Messerotti, M., & Zlobec, P. 1998, *Publications of the Astronomical Institute of the Czechoslovak Academy of Sciences*, 88, 133
- Karlický, M., Zemanová, A., Dudík, J., & Radziszewski, K. 2018, *ApJL*, 854, L29, doi: [10.3847/2041-8213/aaadf9](https://doi.org/10.3847/2041-8213/aaadf9)
- Kopp, R. A., & Pneuman, G. W. 1976, *SoPh*, 50, 85, doi: [10.1007/BF00206193](https://doi.org/10.1007/BF00206193)
- Kotrč, P., Karlický, M., Kupryakov, Y. A., et al. 1999, in *ESA Special Publication*, Vol. 9, *Magnetic Fields and Solar Processes*, ed. A. Wilson & et al., 841
- Krueger, A. 1979, *Introduction to solar radio astronomy and radio physics*, D. Reidel Publ. Comp., Dordrecht, Holland, p. 115

- Lemen, J. R., Title, A. M., Akin, D. J., et al. 2012, *SoPh*, 275, 17, doi: [10.1007/s11207-011-9776-8](https://doi.org/10.1007/s11207-011-9776-8)
- Li, T., Liu, L., Hou, Y., & Zhang, J. 2019, *ApJ*, 881, 151, doi: [10.3847/1538-4357/ab3121](https://doi.org/10.3847/1538-4357/ab3121)
- Liu, C., Lee, J., & Wang, H. 2019, *ApJ*, 883, 47, doi: [10.3847/1538-4357/ab3923](https://doi.org/10.3847/1538-4357/ab3923)
- Liu, C., Prasad, A., Lee, J., & Wang, H. 2020, *ApJ*, 899, 34, doi: [10.3847/1538-4357/ab9cbe](https://doi.org/10.3847/1538-4357/ab9cbe)
- Liu, R., Titov, V. S., Gou, T., et al. 2014, *ApJ*, 790, 8, doi: [10.1088/0004-637X/790/1/8](https://doi.org/10.1088/0004-637X/790/1/8)
- Masson, S., Pariat, E., Aulanier, G., & Schrijver, C. J. 2009, *ApJ*, 700, 559, doi: [10.1088/0004-637X/700/1/559](https://doi.org/10.1088/0004-637X/700/1/559)
- McConnell, D. 1980, *Proceedings of the Astronomical Society of Australia*, 4, 64, doi: [10.1017/S1323358000018816](https://doi.org/10.1017/S1323358000018816)
- . 1982, *SoPh*, 78, 253, doi: [10.1007/BF00151608](https://doi.org/10.1007/BF00151608)
- McLean, D. J., & Labrum, N. R. 1985, *Solar radiophysics : studies of emission from the sun at metre wavelengths*, Cambridge University Press, Cambridge, London, p. 55 and 387
- Melrose, D. B. 1980, *Plasma astrophysics: Nonthermal processes in diffuse magnetized plasmas. Volume 2 - Astrophysical applications*
- . 1997, *ApJ*, 486, 521, doi: [10.1086/304521](https://doi.org/10.1086/304521)
- Norman, C. A., & Smith, R. A. 1978, *A&A*, 68, 145
- Odstrčil, D., & Karlický, M. 1997, *A&A*, 326, 1252
- O'Dwyer, B., Del Zanna, G., & Mason, H. E. 2014, *A&A*, 561, A20, doi: [10.1051/0004-6361/201016346](https://doi.org/10.1051/0004-6361/201016346)
- O'Dwyer, B., Del Zanna, G., Mason, H. E., Weber, M. A., & Tripathi, D. 2010, *A&A*, 521, A21, doi: [10.1051/0004-6361/201014872](https://doi.org/10.1051/0004-6361/201014872)
- Pariat, E., Dalmasse, K., DeVore, C. R., Antiochos, S. K., & Karpen, J. T. 2015, *A&A*, 573, A130, doi: [10.1051/0004-6361/201424209](https://doi.org/10.1051/0004-6361/201424209)
- Pesnell, W. D., Thompson, B. J., & Chamberlin, P. C. 2012, *SoPh*, 275, 3, doi: [10.1007/s11207-011-9841-3](https://doi.org/10.1007/s11207-011-9841-3)
- Poduval, B., DeForest, C. E., Schmelz, J. T., & Pathak, S. 2013, *ApJ*, 765, 144, doi: [10.1088/0004-637X/765/2/144](https://doi.org/10.1088/0004-637X/765/2/144)
- Priest, E. R. 1982, *Solar magneto-hydrodynamics*
- Qiu, J., Longcope, D. W., Cassak, P. A., & Priest, E. R. 2017, *ApJ*, 838, 17, doi: [10.3847/1538-4357/aa6341](https://doi.org/10.3847/1538-4357/aa6341)
- Reid, H. A. S., & Ratcliffe, H. 2014, *Research in Astronomy and Astrophysics*, 14, 773, doi: [10.1088/1674-4527/14/7/003](https://doi.org/10.1088/1674-4527/14/7/003)
- Shibasaki, K. 2001, *ApJ*, 557, 326, doi: [10.1086/321651](https://doi.org/10.1086/321651)
- Simnett, G. M. 1995, *SSRv*, 73, 387, doi: [10.1007/BF00751241](https://doi.org/10.1007/BF00751241)
- Simnett, G. M., & Haines, M. G. 1990, *SoPh*, 130, 253, doi: [10.1007/BF00156793](https://doi.org/10.1007/BF00156793)
- Spicer, D. S. 1977, *SoPh*, 53, 305, doi: [10.1007/BF00160276](https://doi.org/10.1007/BF00160276)
- Sturrock, P. A. 1966, *Nature*, 211, 695, doi: [10.1038/211695a0](https://doi.org/10.1038/211695a0)
- Sych, R., Karlický, M., Altyntsev, A., Dudík, J., & Kashapova, L. 2015, *A&A*, 577, A43, doi: [10.1051/0004-6361/201424834](https://doi.org/10.1051/0004-6361/201424834)
- Tian, H., & Chen, N. H. 2018, *ApJ*, 856, 34, doi: [10.3847/1538-4357/aab15a](https://doi.org/10.3847/1538-4357/aab15a)
- Tian, H., Young, P. R., Reeves, K. K., et al. 2016, *ApJL*, 823, L16, doi: [10.3847/2041-8205/823/1/L16](https://doi.org/10.3847/2041-8205/823/1/L16)
- Wang, H., & Liu, C. 2012, *ApJ*, 760, 101, doi: [10.1088/0004-637X/760/2/101](https://doi.org/10.1088/0004-637X/760/2/101)
- Wyper, P. F., & DeVore, C. R. 2016, *ApJ*, 820, 77, doi: [10.3847/0004-637X/820/1/77](https://doi.org/10.3847/0004-637X/820/1/77)
- Wyper, P. F., DeVore, C. R., Karpen, J. T., & Lynch, B. J. 2016, *ApJ*, 827, 4, doi: [10.3847/0004-637X/827/1/4](https://doi.org/10.3847/0004-637X/827/1/4)
- Zuccarello, F., Romano, P., Farník, F., et al. 2009, *A&A*, 493, 629, doi: [10.1051/0004-6361:200809887](https://doi.org/10.1051/0004-6361:200809887)

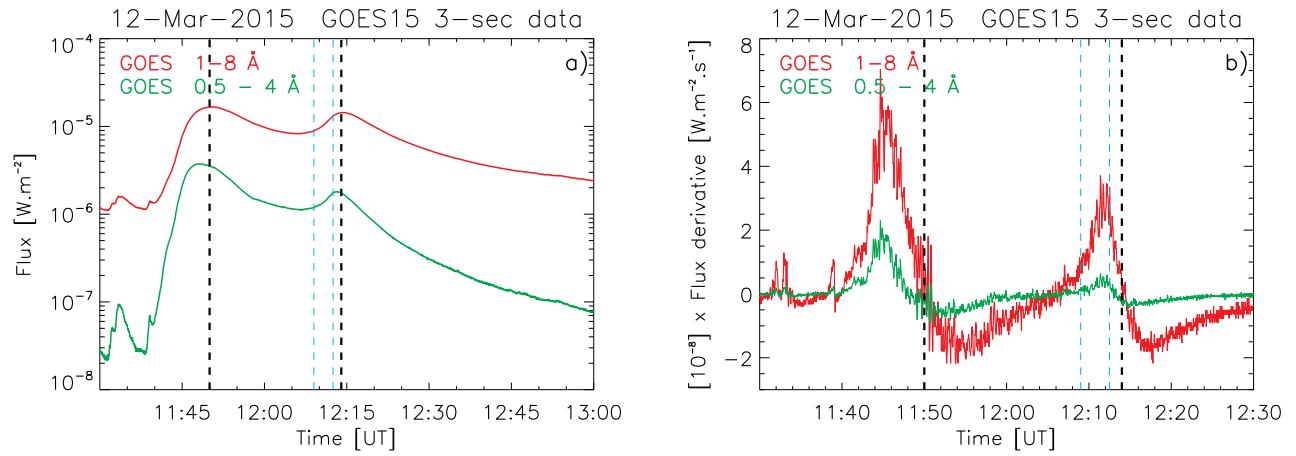


**Figure 1.** (a) Soft X-ray light curves for two M-class flares on 2015 March 12 for both GOES15 channels and (b) their derivatives. The black dashed lines show maxima of the flares and the dashed blue lines indicate the time interval when SPDBs were observed (12:09:00–12:12:30 UT).

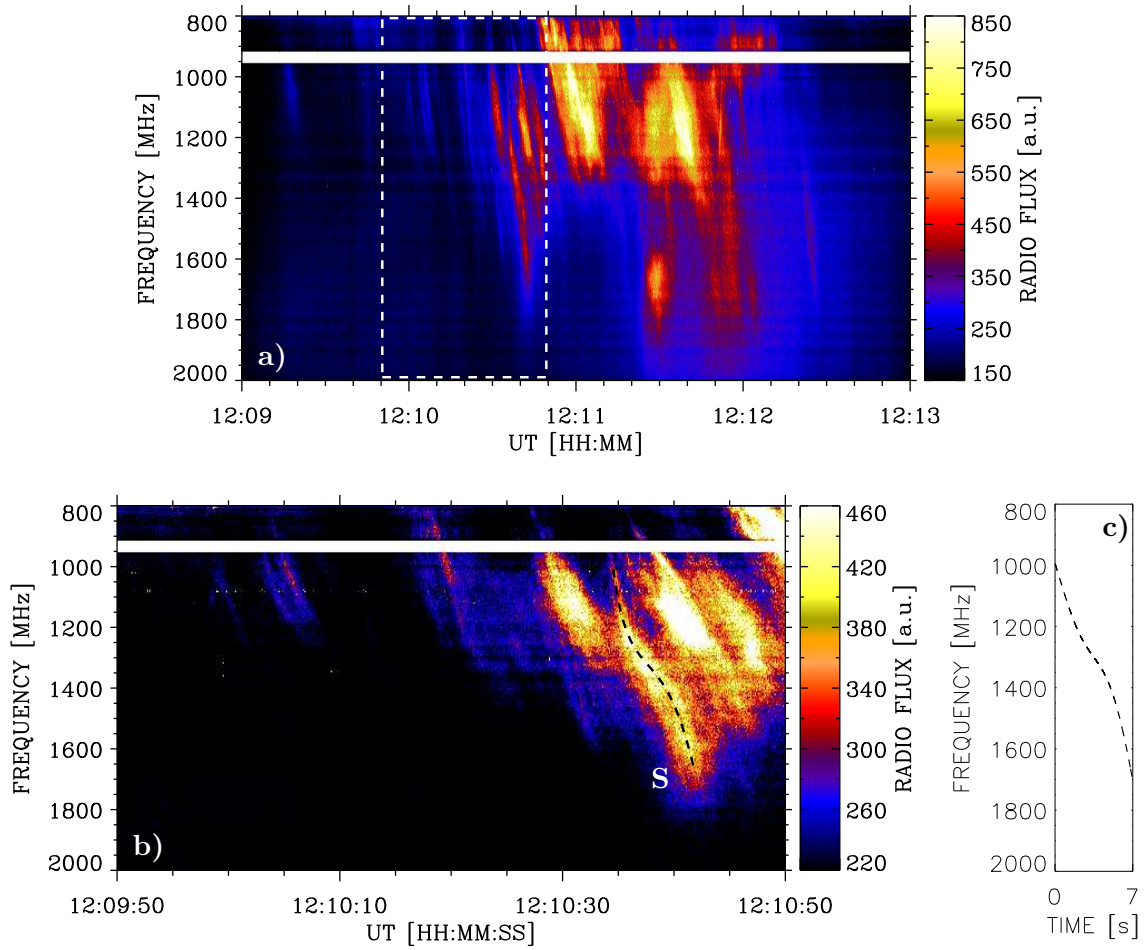


**Figure 2.** Panel (a) shows the 800-2000 MHz radio spectrum observed at 12:09–12:13 UT during the 12 March 2015 flare by the Ondřejov radiospectrograph. The white narrow horizontal band at about 950 MHz means no data. Panel (b) is the zoom of the spectrum during the 12:09:50 - 12:10:50 UT time interval (dashed-line box in Panel (a)). The dashed line and the letter S point out the S-like form of Burst S. Panel (c) shows the simulated S-like form of the Burst S.



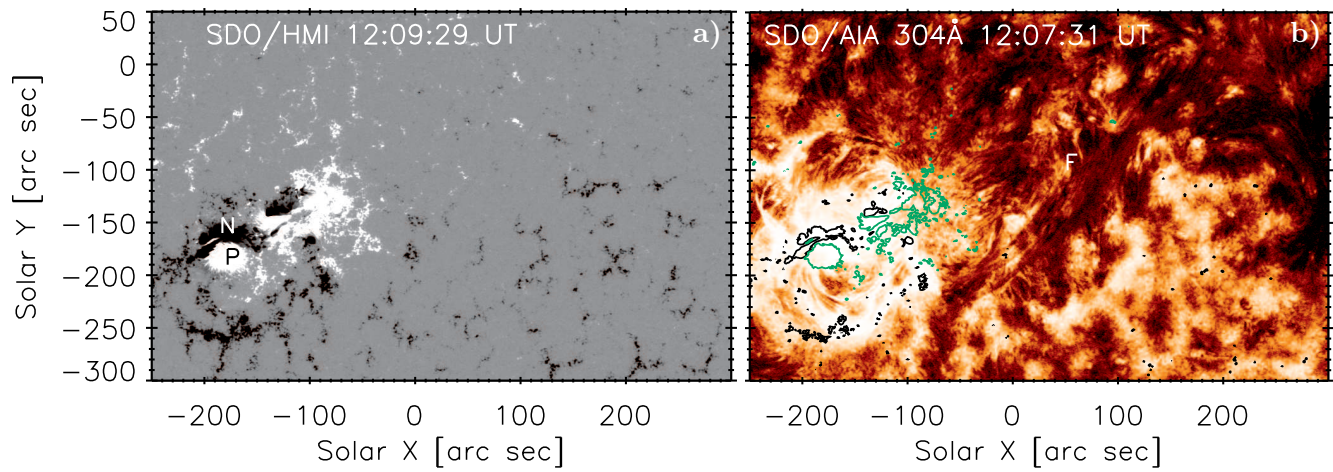


**Figure 3.** Panel (a) shows the *SDO*/HMI line-of-sight magnetic field at 12:09:29 UT with a big spot of positive polarity P and negative polarity N. Panel (b) shows the histogram equalized image of the *SDO*/AIA 304 Å filter showing the location of the dark filament marked by F. Contours of the line-of-sight magnetic field are overlaid in green and black ( $\pm 500$ G, respectively).

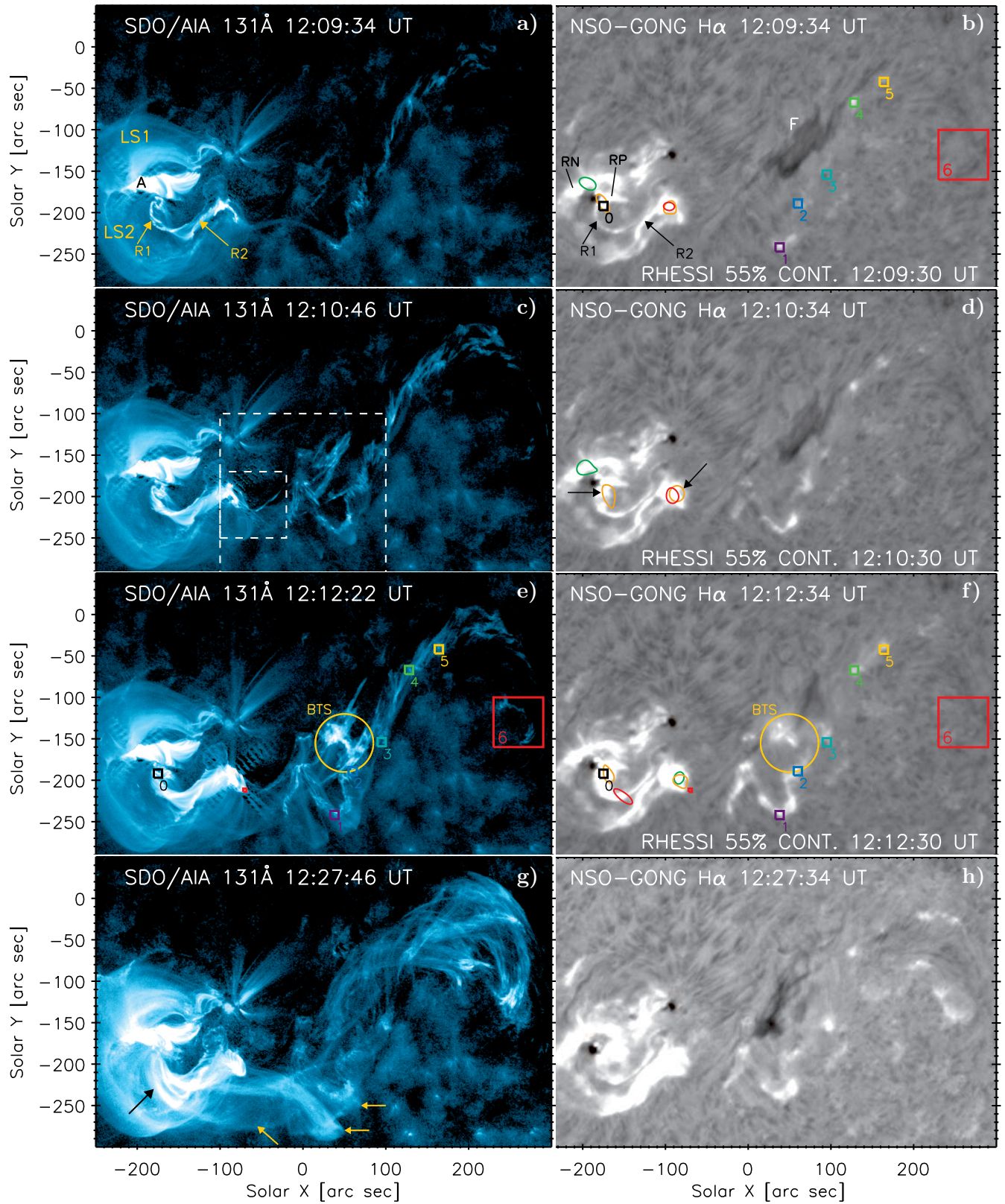


**Figure 4.** Evolution of the M1.4 flare. X-ray sources are shown by green (6–12 keV), orange (12–25 keV), and red (25–50 keV) contours. Those located in hooks of R1 and R2 are marked by black arrows in (d). Colored Regions 1–6 show locations of brightenings along the F and Region 0 is located at the hook of R1. Large dashed rectangle in (c) is FOV for Figures 5, 6, and 9, the small one is FOV for Figure 7. Tiny red square marks the position of the cusp (see Figure 10(a)). The arrows in (g) point to the flare loops, see Sec. 3.2. An animation of this figure is available. It contains 131Å and H $\alpha$ . Both run approximately from 12:00–13:00 UT. Ribbons R1, R2 and Regions 0–6 are labeled there.

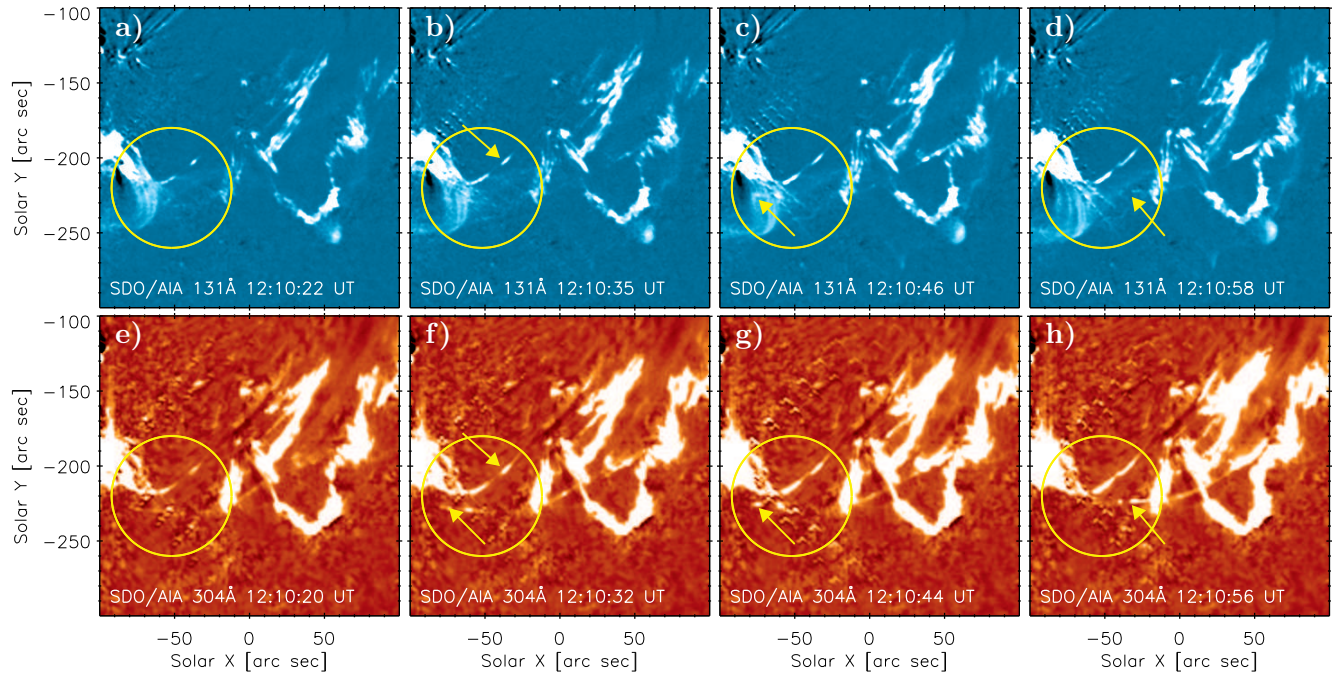


**Figure 5.** Detail of the cusp and plasma ejection during the Burst S. (a)–(d) Base difference images in *SDO/AIA* 131 Å filter with a base image at 11:30:10 UT. (e)–(h) Base difference images in *SDO/AIA* 304 Å filter with a base image at 11:30:08 UT. For an explanation see Sec. 3.2.1.

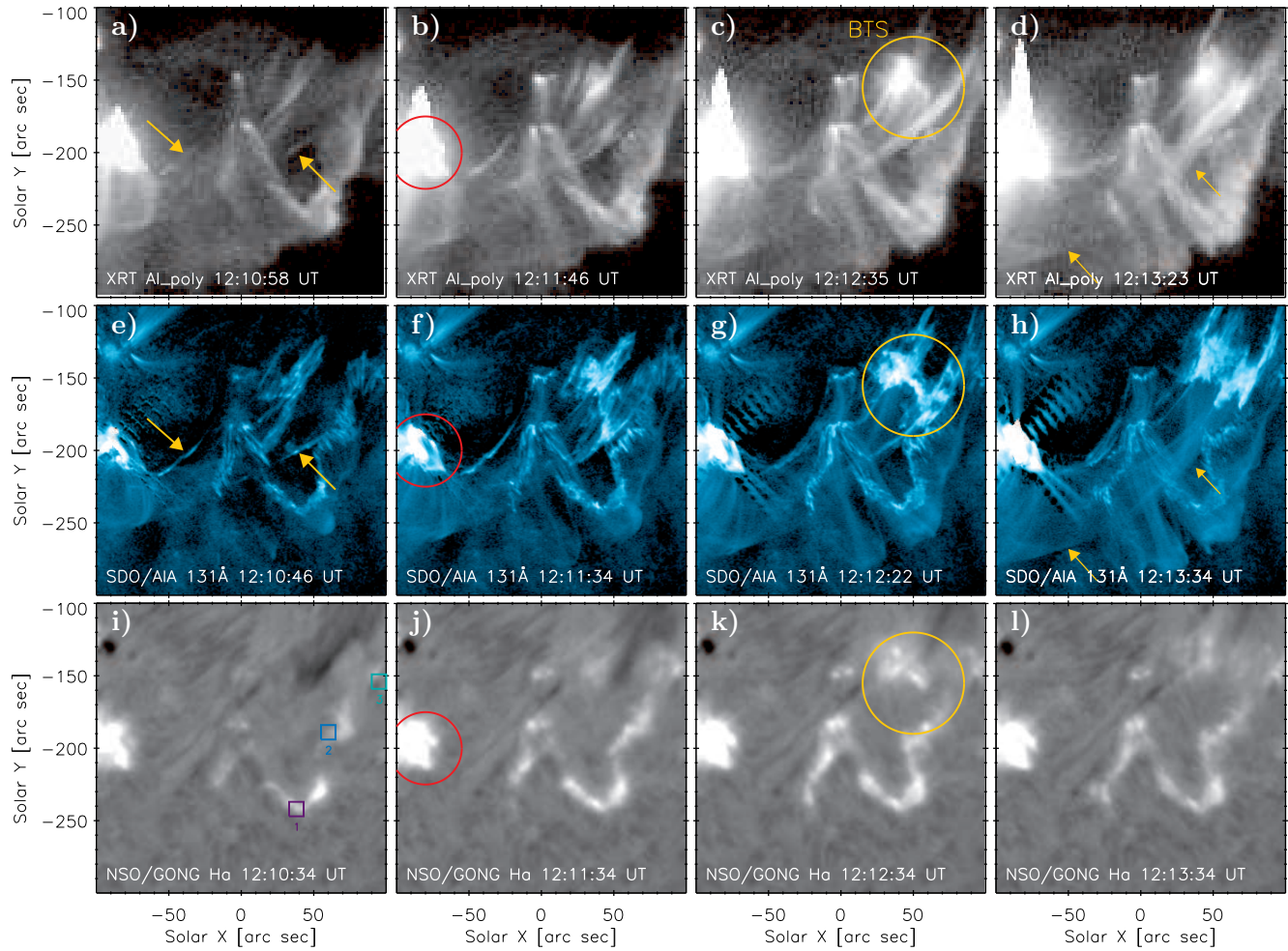


**Figure 6.** Zoomed view of plasma ejection toward the preexisting filament and formation of BTS. The FOV is the same as in Figure 5. Top row (a–d) shows formation of the cusp and BTS in *Hinode*/XRT Al<sub>poly</sub> filter. Middle row of (e–h) shows this evolution in *SDO*/AIA 131 Å images. Bottom row (i–l) shows the same but in GONG H $\alpha$  filtergrams. Colored squares in (i) show positions of brightenings 1–3 along the F. Location of the cusp is marked in red circles and the BTS is marked by yellow circles. Arrows in (a) and (e) show plasma coming out of the cusp, forming new flare loops after the Burst S. Arrows in (d) and (h) show faint tails of hot plasma behind the BTS.

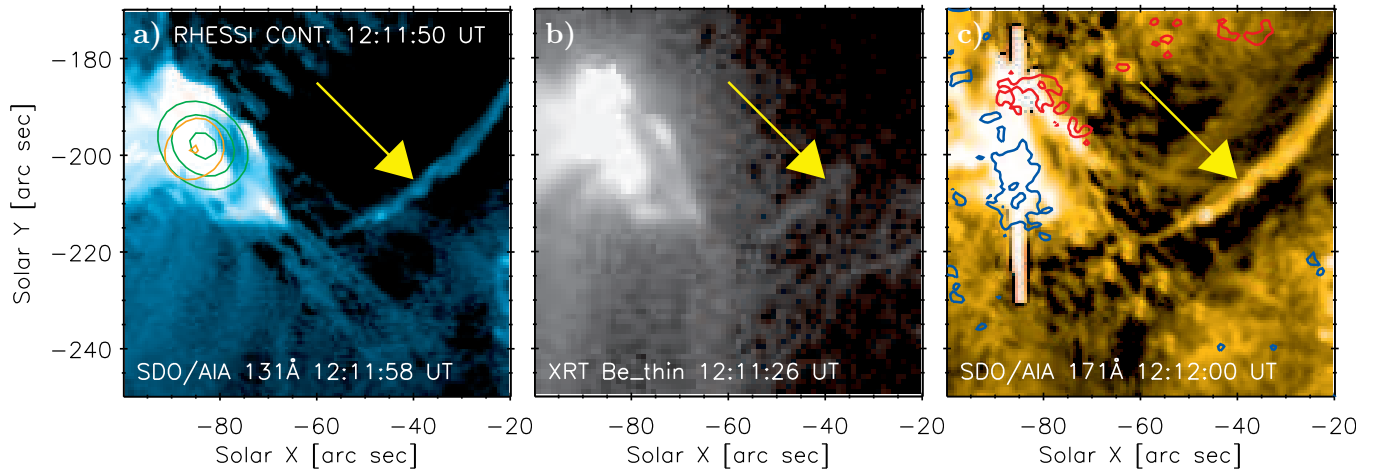


**Figure 7.** Detailed view of the cusp. Hot channels, *SDO/AIA* 131 Å (a) and *Hinode/XRT* Be\_thin (b) filters, show the structure in the cusp. The 55, 75, and 95% contours on panel (a) mark the position of the *RHESSI* source at 12:11:50 UT (green 6–12 keV, orange 12–25 keV). Panel (c) shows the area of the cusp in the 171 Å *SDO/AIA* filter. Contours depict *SDO/HMI* line-of-sight magnetic field of  $\pm 300$  G (red/blue, respectively). The arrows point to the flare loop coming out of the cusp, see Sec. 3.2.1. The FOV for this figure is shown by the small dashed rectangle in Figure 4(c).

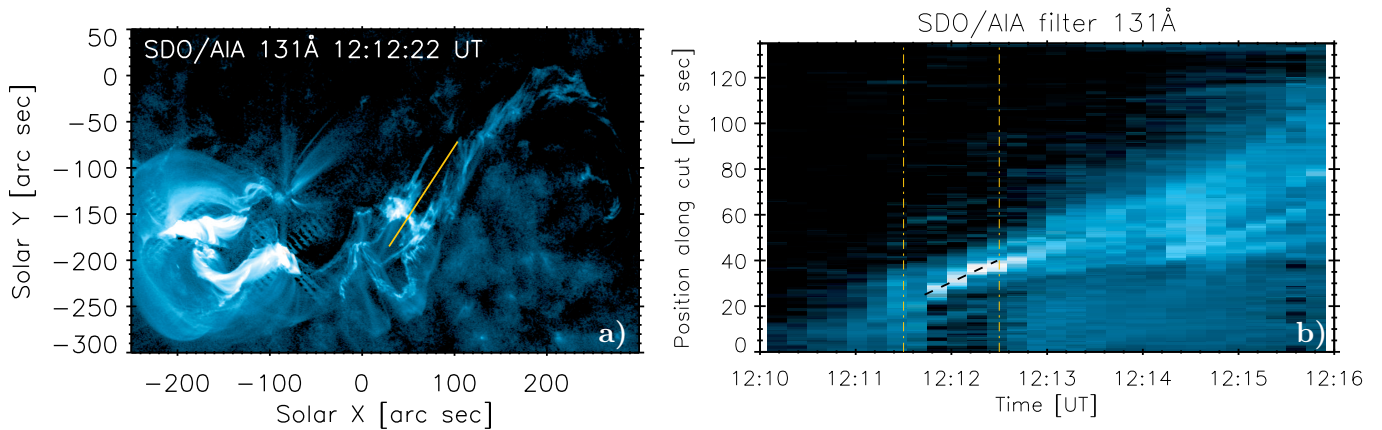


**Figure 8.** Velocity estimation of BTS. The yellow line running across BTS in (a) shows the cut from where the time-distance plot in (b) was constructed. Dash-dotted lines mark the 12:11:30–12:12:30 UT time interval when the BTS was narrow. The slope of the bright ridge (black dashed line) was measured to estimate its velocity.

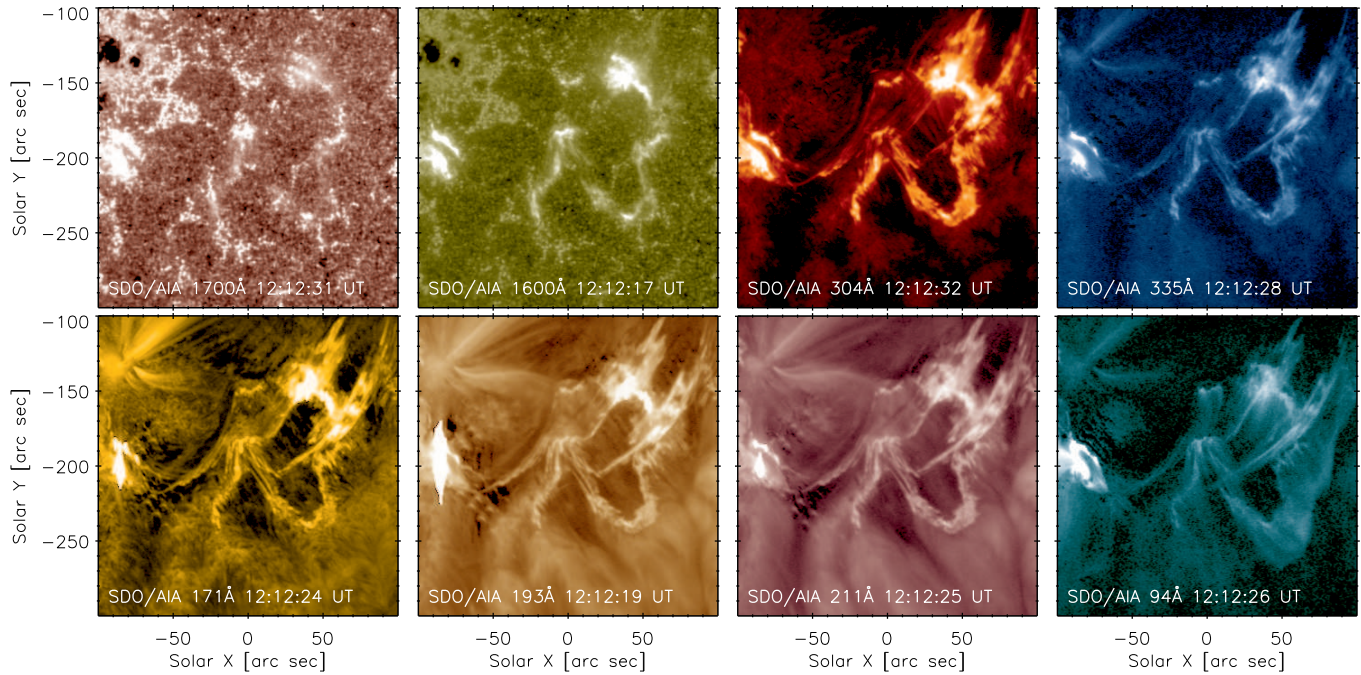


**Figure 9.** Multi-thermal BTS as seen in other *SDO/AIA* UV/EUV filters at about 12:12:30 UT. The FOV is the same as in Figure 6.

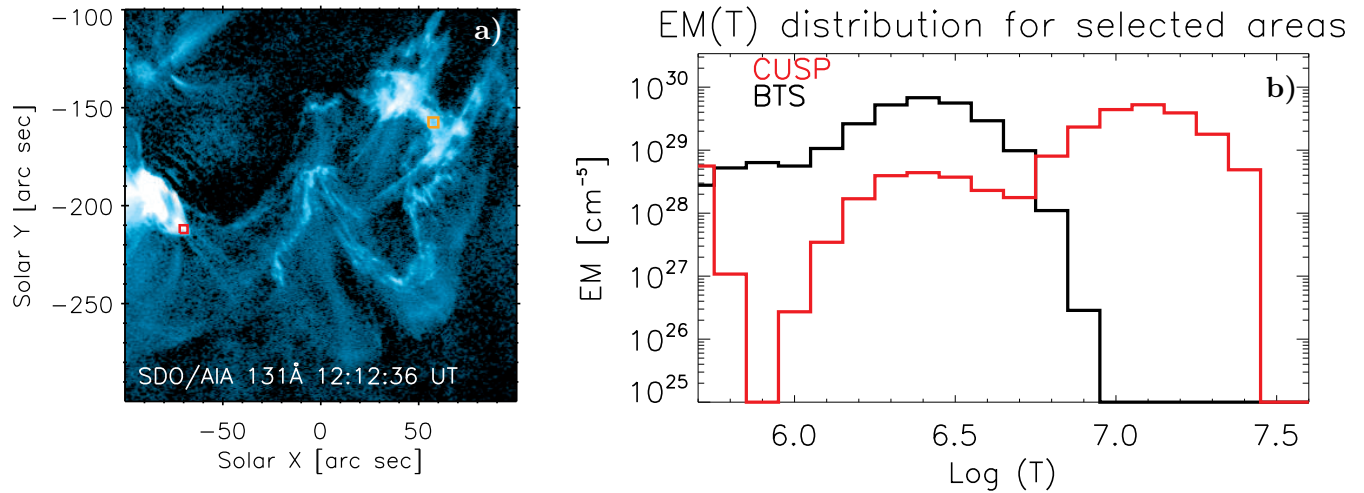


**Figure 10.** Distribution of emission measure per temperature bin at about 12:12:36 UT, calculated using *SDO/AIA* filters. (a) 131 Å filter image showing the areas selected in cusp (red square) and in BTS (orange square). (b) Emission measure distribution per temperature bin for cusp (red) and BTS (black).

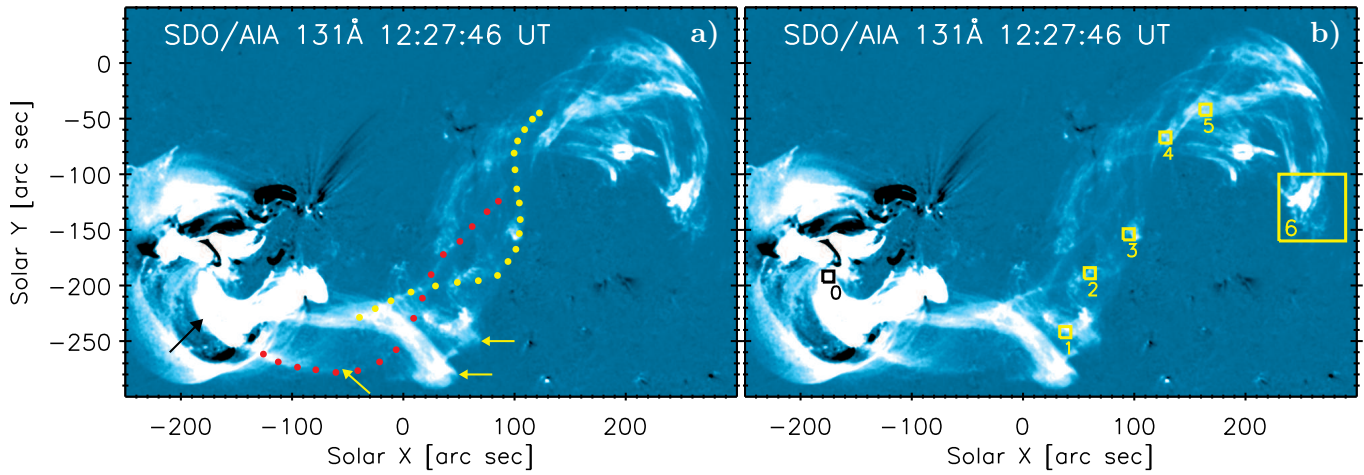


**Figure 11.** Base difference of  $131 \text{ \AA}$  *SDO/AIA* image at 12:27:46 UT with a base image taken at 11:30:10 UT. The original image is in Figure 4(g). Panel (a) shows newly created flare loops (arrows) and newly created twisted loops (red and yellow dots). (b) The same image as (a) but showing positions of brightenings observed along the F (Regions 1–6) and Region 0, which was located at the hook of R1.

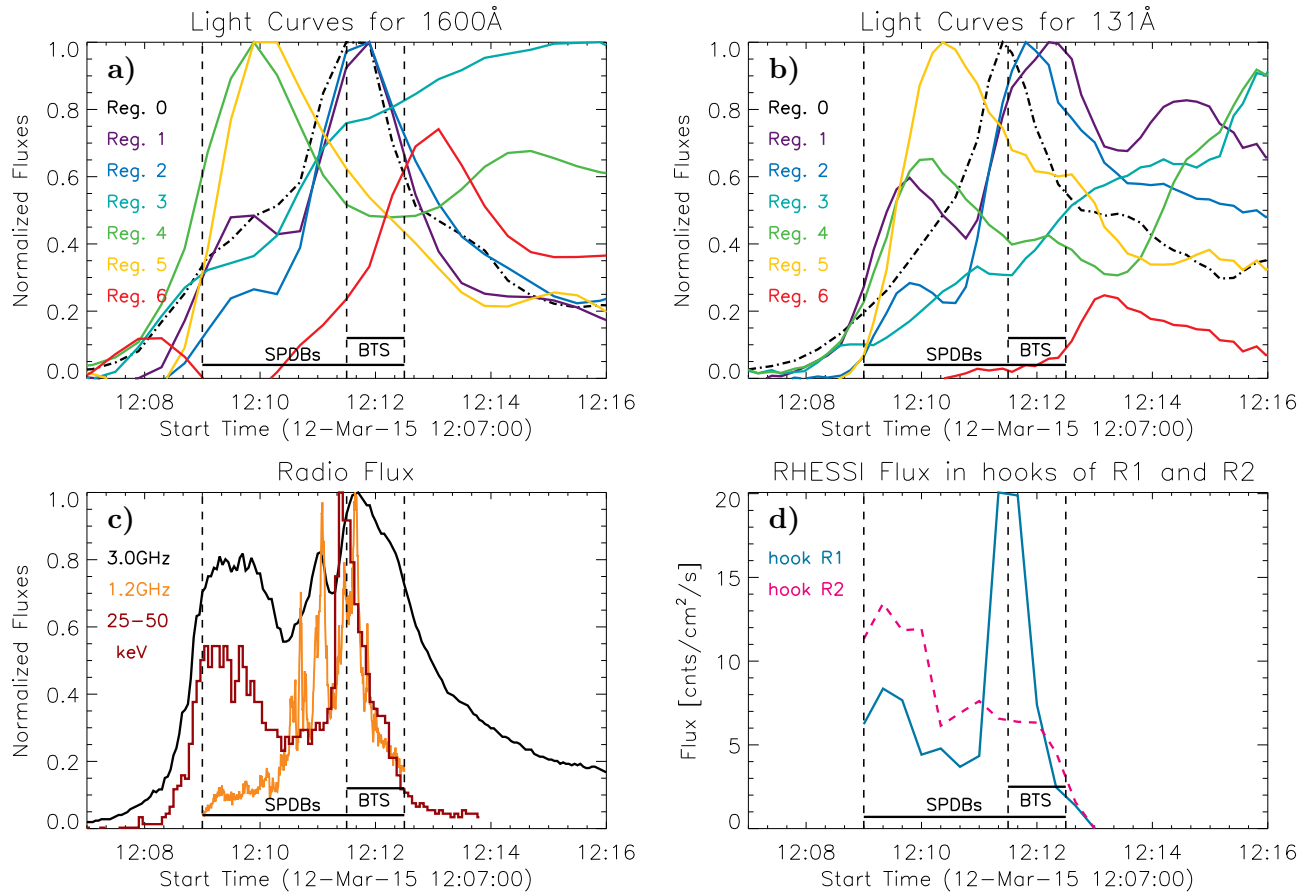


**Figure 12.** The light curves. (a) Normalized 1600 Å light curves for brightenings located along the F and for the Region 0 located in the hook of R1. (b) The same as in (a) but for the 131 Å filter. (c) Light curves in radio 3 GHz (black), 1.2 GHz (orange), and hard X-ray emission in 25–50 keV (brown). (d) Light curves for hard X-ray sources observed in the hooks of R1 (blue) and R2 (purple) in *RHESSI* 25–50 keV channel. Vertical dashed lines and their horizontal labels show time intervals when SPDBs (12:09:00–12:12:30 UT) and BTS (12:11:30–12:12:30 UT) were observed.